An intelligent converter and controller for electric vehicle drives utilizing grid and stand-alone solar photovoltaic power generation systems

G. Saikiran Reddy[1], M. Premkumar[1], Suraj Ravi[1], Laith Abualigah[2-8]

[1]Department of Electrical and Electronics Engineering, Dayananda Sagar College of Engineering, Bengaluru, India
[2]Department of Computer Science, Prince Hussein Bin Abdullah Faculty for Information Technology, Al al-Bayt University, Mafraq, Jordan
[3]Department of Electrical and Computer Engineering, Lebanese American University, Byblos, Lebanon
[4]Hourani Center for Applied Scientific Research, Al-Ahliyya Amman University, Amman, Jordan
[5]MEU Research Unit, Middle East University, Amman, Jordan
[6]Applied Science Research Center, Applied Science Private University, Amman, Jordan
[7]School of Computer Sciences, Universiti Sains Malaysia, Pulau Pinang, Malaysia
[8]School of Engineering and Technology, Sunway University Malaysia, Petaling Jaya, Malaysia

Article Info

ABSTRACT

In this study, a battery energy management system for electric vehicle (EV) applications is proposed with a standalone photovoltaic (PV) source and controlled based on the availability of grid, PV source, load consumption, and energy stored in the battery. This paper proposes a single-ended primary-inductance converter (SEPIC) DC-DC converter for charging the battery through the utility and PV source that provides good load regulation. The bidirectional nature of the proposed DC-DC converter provides the charging and discharging of the EV battery in the succeeding modes of operation, i) grid-tied charging, ii) PV-tied charging, iii) discharging to the load in the absence of utility and PV source, and iv) regenerative braking. An improved perturb and observe-based maximum power point tracking (MPPT) algorithm is proposed to track the maximum power from the PV source. In addition, to handle the four modes of operation, a dedicated controller is also proposed. Firstly, the proposed system is validated using MATLAB/Simulink software by considering different operating conditions, and the performance is compared with the traditional MPPT algorithms. Finally, the effectiveness of the suggested system is validated through an experimental prototype. The result proved the superiority of the converter and controller over the traditional systems.

Corresponding Author:

M. Premkumar
Department of Electrical and Electronics Engineering, Dayananda Sagar College of Engineering
Bengaluru, Karnataka 560078, India
Email: mprem.me@gmail.com

Nomenclature

I_s	: Photocurrent of the cell (A)
I_d	: Saturating diode current (A)
n	: Ideality factor of the diode
R_s	: Series equivalent resistance (Ω)
R_p	: Shunt equivalent resistance (Ω)
V_{out}	: Output voltage of the SEPIC converter

V_{in} and $V_s s$	: Input voltage to the converter
V_{Cs}	: Voltage across the coupling capacitor of the SEPIC converter
V_{L1} and V_{L2}	: Voltage across the inductors L1 and L2, respectively
L_m	: Magnetizing inductance (H)
i_s	: Source current (A)
$א$	: Flux linkage
F_s and f_L	: Switching frequency and supply frequency, respectively, in Hz
P_s	: Power flow on the grid side (W)
d_1	: Pulse width of MOSFET switch S_{a1}
V_b, I_b, and P_b	: Battery voltage (V), current (A), and power (W), respectively
R_L	: Load resistance (Ω)
V_{PV} and P_{PV}	: PV voltage and power, respectively
V_{hv} and C_{hv}	: Voltage and capacitance at the high voltage side of the converter

1. INTRODUCTION

The automation industry's primary concerns are lowering greenhouse gas emissions and the swift depletion of conventional fuels used in automobiles. Electric vehicles (EVs), which use batteries in place of traditional sources of energy, were developed as a substitute fuel that produces fewer emissions of carbon dioxide. Energy is still needed to power the batteries so that automobiles can run without releasing greenhouse gases into the atmosphere. In EVs, the EV is powered by renewable energy sources like photovoltaic (PV) and fuel cells, which are also used to store any extra energy for future use. However, storing hydrogen gas for fuel cells makes the design as intricate as lithium-ion in practice. Although lithium-ion batteries [1]–[4] outperform previous battery types in terms of performance, there is still potential for development in terms of thermal properties, which can impact the overall system when utilized for extended periods. Fast charging procedures are employed to charge the batteries for effective operation, resulting in decreased capacity and battery longevity. So, to charge the batteries without increasing C-rates, optimization approaches are required, and estimating of state of charge (SOC) is crucial for such strategies [5], [6]. By examining the battery's open circuit voltage at various SOCs, a lookup table is created that is utilized to calculate SOC while the vehicle is in operation. The proposed Luo converter to drive the switched reluctance motor (SRM) for pumping applications [7]. As the PV functions with a maximum power peak (MPP), its operation is based on the procedures of charging the battery, and the power produced is provided to the load [8], [9]. It provides continuous current and voltage through the inductor and capacitor to drive the SRM and soft starting is done by an appropriate assortment of initial duty cycles besides step change of duty ratio by the maximum power point tracking (MPPT). The efficiency of the system reduces with the reduction of solar irradiance. The proposed regulation of grid voltage by online tap changing transformer [10]. This combination of mechanical and power electronic switches is used for load regulation of the system. The mechanical switches operate during steady-state conditions, and power electronic switches operate during the tapping process, and this is done for real and reactive power compensation in high voltage, high power systems. Mouli *et al.* [11] and Shariff *et al.* [12] have proposed a 10 kW EV charging system using a three-port converter with bidirectional functionality as both vehicle-to-grid (V2G) and grid-to-vehicle (G2V) modes are implemented. A pulse-width modulation (PWM) boost rectifier cascaded with a bidirectional DC-DC converter [13] has been proposed for charging the electric vehicle with power factor improvement. However, huge battery storage is required as the PV provides energy in the daytime only. They proposed an integrated EV charging system with PV and wind energy sources with voltage regulation control, providing DC voltage regulation by charging and discharging the batteries depending on loading conditions [13]. Medium-level and high-power devices or equipment have been reported to charge batteries utilizing non-isolated architectures of the DC-DC converters. With lower and medium DC-link voltages, the interleaved boost converters and the traditional boost converters are employed for charging EV batteries [14]–[16].

Extreme fast charging techniques are reviewed to meet the growing demand for electric vehicles. Solid-state transformers can be utilized in place of conventional power line frequency transformers. Modular DC-DC converters are proposed to allow different battery technologies to be linked to drive inverters operating independently from each other. Wide-bandgap power semiconductors are used in order to enable high switching frequencies and reduce the size of passive elements. This leads to a reduction of losses, in particular at light loads. However, proper passive elements are to be designed, and even slight deviation will lead to overshoots of DC voltage and stray capacitances in the switches, resulting in a common mode current. DC micro grid-based electric vehicle charging system is offered to increase productivity and reduce charging time. Mahmud *et al.* [17] proposed an algorithm which provides charging and discharging of vehicles based on the peak loads by coordinating PV sources, battery energy storage systems and EVs. The charging of an

EV depends upon the distance to be travelled and the SOC of the battery. Monteiro *et al*. [18] proposed a multiport converter which integrates PV, EV and grid in which G2V, V2G, PV2G, and PV2V modes are achieved using the proposed predictive control structure. Singh *et al*. [19] proposed an integrated-on board charger in which the external sensors are not required for power factor correction due to nonlinear control techniques. Venkata and Williamson [20] proposed an onboard charger with buck and boost modes, and a dual-mode control strategy is used for voltage regulation and power factor correction and enables the smooth transition between the modes. Jain *et al*. [21] proposed an incremental conductance-based MPPT algorithm in place of perturb and observation (P&O) algorithm, and the incremental conductance (INC) procedure is more competent and possesses higher tracking speed over varying solar irradiations. The INC-based MPPT technique is used for its potency and provides better performance under the varying condition of solar irradiation. It is based on the slope of the PV power characteristics being zero in the maximum power point, either positive or negative. It is similar to the working of the P&O-based MPPT technique, and it requires voltage and current sensors once the MPP is achieved. Further calculation of PV power is not required as the oscillations are minimized, and the step size of the increment decides the tracking speed of the MPPT. The algorithms track the peak power and might settle on local peak power instead of global peak power.

In [22], grey wolf optimization (GWO) technique is proposed under partial shading conditions (PSCs), and it is tried with multiple peaks, and its tracking performance is compared with that of two MPPT algorithms, namely P&O-MPPT and improved particle swarm optimization. A new algorithm termed as firefly algorithm was proposed [23] to track the global maximum point. However, the computation speed is reduced, and the convergence time is increased. A new technique is presented in [24], in which fractional chaos maps are integrated into the algorithm to increase accuracy and reliability. It can follow the input data provided with minimized deviation, increased rate of convergence, and requires minimum time for computation. In [25], a wind-driven optimization-based MPPT is presented, and its effectiveness is contrasted with that of seven other algorithms, such as differential evolution, genetic algorithm, and particle swarm optimization. In [26], without considering the PV cell's temperature or the amount of solar irradiance, the genetic algorithm approximates the PV current and PV voltage at the maximum power point. It provides stability and reduces the oscillations around the maximum power point as it is not concentrating on power deviations. A modified cat swarm optimization is proposed to realize global MPPT for the PV system. In [27], modified cat swarm optimization is proposed, which deals effectively with the partial shading conditions of the PV system. The accuracy and tracking speed increase by using this MPPT. In [28], an analytical approach is performed by tracking maximum power under shaded conditions. It is simple and quick, and the accuracy in predicting the maximum power is improved by integrating the functionality of reverse blocking and bypass diodes in the circuit model. Also, the proposed technique could be utilized for any number of series/parallel combinations under partial conditions. In [29], a modified hybrid MPPT technique is proposed by combining the traditional evolutional algorithms, such as differential evolution and particle swarm optimizer. Each algorithm is employed to overcome the drawbacks of the other algorithm, and also it is simple and can be implemented in low-cost controllers.

In [30], various algorithms, such as P&O, INC, particle swarm optimization, and adaptive fuzzy are studied and compared with each other under single and multiple global peaks caused by partial shading under various configurations of a DC-DC converter. A new flower pollination algorithm (FPA) method combined with P&O is proposed in [31]. In this, a new switching technique is used by integrating both FPA and P&O algorithms. The P&O takes over once the FPA algorithm estimates global power peaks. Hence, the switching losses are reduced. In [32], the deep reinforcement learning concept addresses solutions for the MPPT issues under partial shading conditions. A model-free reinforcement learning algorithm is used to increase the tracking efficiency of MPPT. An adaptive neuro-fuzzy inference system and particle swarm optimization are hybridized to formulate a hybrid MPPT algorithm [33] to get maximum power with zero oscillation tracking at a higher tracking speed. This method needs no sensor to measure the cell's irradiance and temperature. They proposed combining the P&O algorithm and adaptive proportional integral derivative (PID) controller to track the maximum power. The gains of the adaptive PID controller are designed for various solar irradiations; hence, the efficiency is increased under all conditions, and the tracking speed is improved [34]. They suggested a simplified hybrid firefly and neighborhood attraction firefly-based MPPT that offers higher convergence velocity, fast-tracking, accurate responses, higher efficiency, and can track the global maximum power point in shady areas and through various operating conditions [35]. Based on a thorough literature study, this paper proposed an effective converter based on SEPIC topology and an intelligent controller to handle different operating conditions and loads. In addition, a modified P&O algorithm is also proposed to handle the partial shading conditions. Four different modes of the suggested system are deeply examined, and experimental findings are provided for all modes of operation.

It is proposed to design and implement a DC-DC SEPIC converter for battery charging applications. It consists of a solar array at the source side, and the output of the converter is connected to a battery. Together with the change in current (dI), along with the voltage and power conditional phases, it is suggested

as a way to enhance the MPPT algorithm. Further, a closed loop controller like a proportional integral (PI) controller is designed and simulated to maintain the output voltage and current constant for a specific valve. The primary contribution of this paper is as follows: i) Design and develop SEPIC-based DC-DC converter for electric vehicle battery charging; ii) Design and develop intelligent controllers for controlling the operation of the converter in the charging and discharging modes of the EV battery; iii) Design and develop a new MPPT algorithm based on the P&O algorithm; iv) Verification of theoretical analysis using simulation and experimental studies; and v) Comparison of the converter operation between the proposed P&O and other traditional algorithms.

This paper is organized as follows. The proposed topology is provided in section 2. The design approach of the suggested converter topology is discussed in section 3. The different MPPT techniques, including the proposed modified P&O algorithm, are discussed in section 4. Section 5 analyzes the controller strategy for various modes of operation. The simulation and experimental results are provided in section 6. The conclusions are provided in section 7.

2. PROPOSED EV BATTERY CHARGING SYSTEM

The suggested EV strategy with a photovoltaic energy function is in four phases: i) grid charging, ii) PV charging, iii) propulsion, and iv) regenerative braking. It includes a built-in SEPIC converter, a PV source, a battery for energy storage, as well as load parameters like power consumed, power generated, voltage, and battery state of charge. The SEPIC DC-DC converter, along with the controller, regulates the load voltage and supplies a pulse to the converter to function for both buck and boost modes. The auxiliary toggles manage the operational modes. Figure 1 presents the suggested system for recharging the batteries of electric vehicles.
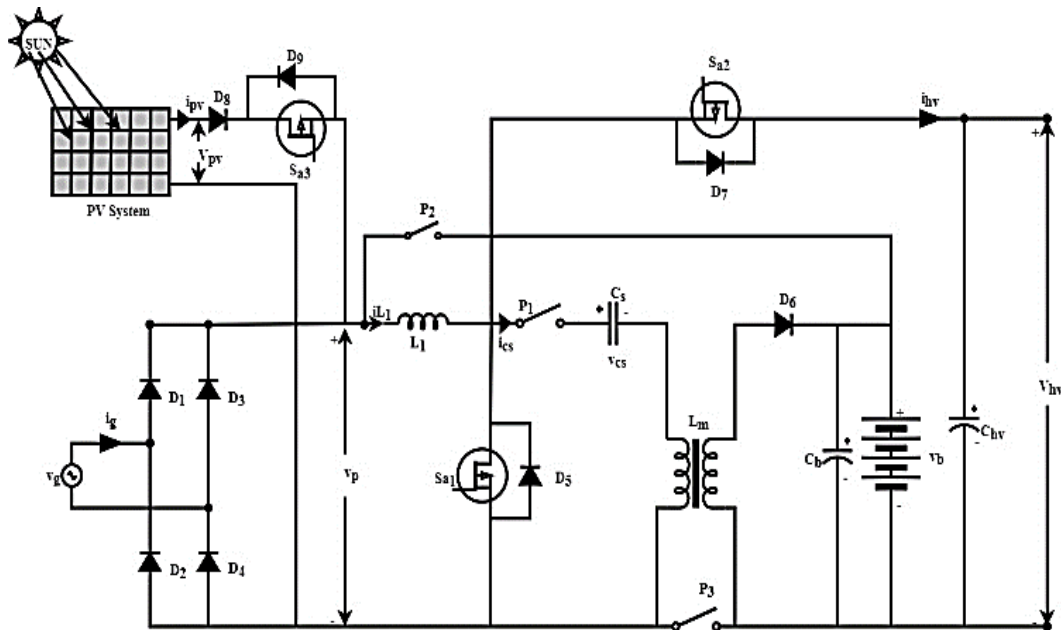

Figure 1. Schematic diagram of the suggested EV system

2.1. PV cell modelling

This study uses PV panels of 12 V and 100 W for power production. Figure 2 shows a single-diode illustration of a PV cell. The following provides a five-parameter PV cell model [36]:

$$I = I_s - I_d \left(e^{\frac{V + IR_S}{nV_T}} - 1 \right) - \frac{V + IR_S}{R_p} \tag{1}$$

where R_p is the shunt resistance (Ω), R_s is the series equivalent resistance (Ω), the ideality factor for diodes is n (ranges from 1 to 2), I_d is saturating diode current (A), I_s is photocurrent (A), $V_T = kT/q$ denotes the thermal voltage, q denotes the electron charge, k denotes the Boltzmann constant, and T denotes the absolute temperature of the cell.
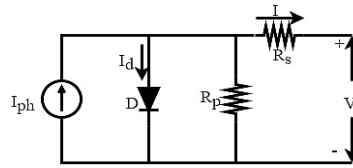
Figure 2. Single diode model of solar cell

2.2. SEPIC converter

The circuit diagram of a SEPIC-based DC-DC converter is shown in Figure 3. The single-ended primary-inductor converter is a type of DC-DC converter that allows the electrical potential (voltage) at its output to be greater than, less than, or equal to that at its input. The SEPIC converter has two modes of operation. When the pulse is high, the MOSFET turns on. Capacitor C1 and input voltage V_{in} charge the inductors L1 and L2. The output capacitance C2 supplies the load when the diode is not conducting. When the gate pulse is zero, the power switch turns off, enabling the current through the inductor to circulate through the load and the capacitors get charged. Longer charge durations lead to increased inductor voltage; hence the load voltage rises as the duty cycle does. The duty cycle can be calculated using (2).

$$D = \frac{V_{out}}{V_{in}+V_{out}} \tag{2}$$

Where V_{out} signifies the load voltage and V_{in} represents the source voltage.

- Mode 1: The capacitor C2 is discharged whenever the switch is ON, while the inductors L2 and L1 are charged. The voltage equation for this mode is provided in (3). The equivalent circuit for the SEPIC converter for mode 1 is shown in Figure 4.

$$V_{in} = V_{L1} + V_{Cs} + V_{L2} \tag{3}$$

Because the average voltage of V_{Cs} is equal to V_{in}, the expression for the voltage across the inductor is given as (4).

$$V_{L1} = V_{L2} \tag{4}$$

- Mode 2: When the switch is OFF, the inductors start discharging, and the capacitor C2 gets charged. The output voltage for mode 2 is provided in (5). The equivalent circuit for the SEPIC converter for mode 2 is shown in Figure 5.

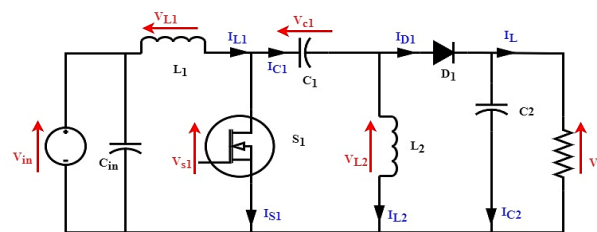$$V_{out} = V_{Q1} - V_{in} \tag{5}$$
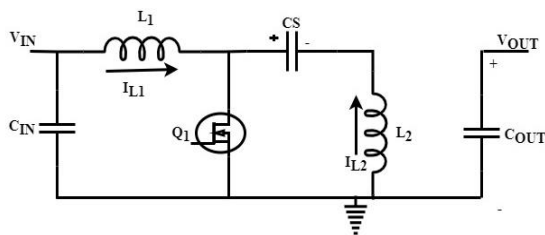

Figure 3. Schematic of a SEPIC-based DC-DC converter

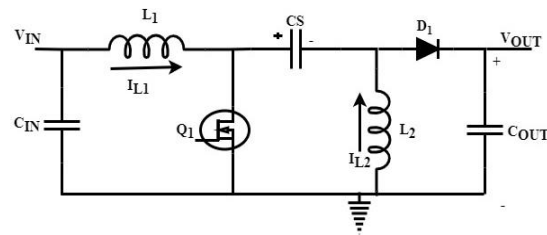
Figure 4. Equivalent circuit for SEPIC converter - Mode 1

Figure 5. Equivalent circuit for SEPIC converter - Mode 2

2.3. Modes of operation of the proposed converter

The conventional SEPIC converter is modified in such a manner that it consists of four ports, two at the input side (AC supply and PV) and two at the output side (battery and load). When the AC supply is available, it charges the battery; otherwise, PV charges the battery. When the vehicle is moving, the battery discharges and supplies the motor. When braking is applied, the energy from motor windings is fed back to the battery. The proposed converter operates in four modes which are provided as follows:

- Mode 1: Grid charging mode

In this mode, the PV module is not included. P_1 is ON, while P_2 and P_3 remain OFF. The L_m and inductor L_1 are charged when S_{a1} is turned on, and in Figure 6, the inductor's current path is shown with bolder lines. The capacitor C_b powers the storage device in this state. The energy of the L_m and L_1 has been released, C_s get charged, and the load is provided as S_{a1} is turned OFF.

- Mode 2: PV charging mode

When the PV power reaches a specified threshold, the suggested system switches to this operation. During this mode, the switch S_{a3} is in the ON position. The converter operation in this mode uses logic comparable to mode 1. The MPPT operates and charges the battery with all of its available power. In mode 2, the maximum power differs depending on the fluctuating sun irradiation. The analogous circuit for this mode is shown in Figure 7. The PV module can power other individual batteries when EV charging is not necessary for the objective. Thus, the switch S_{a2} improves the use of the PV module in such circumstances.
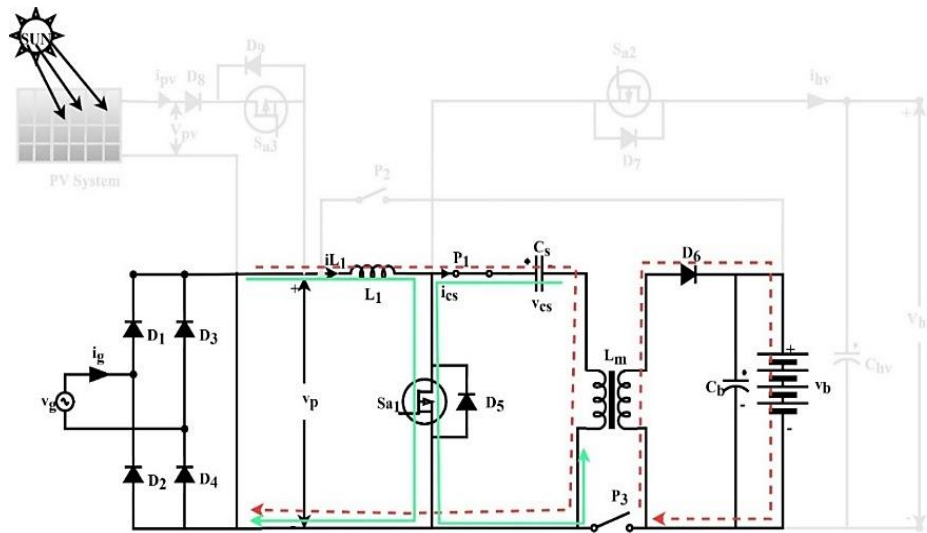

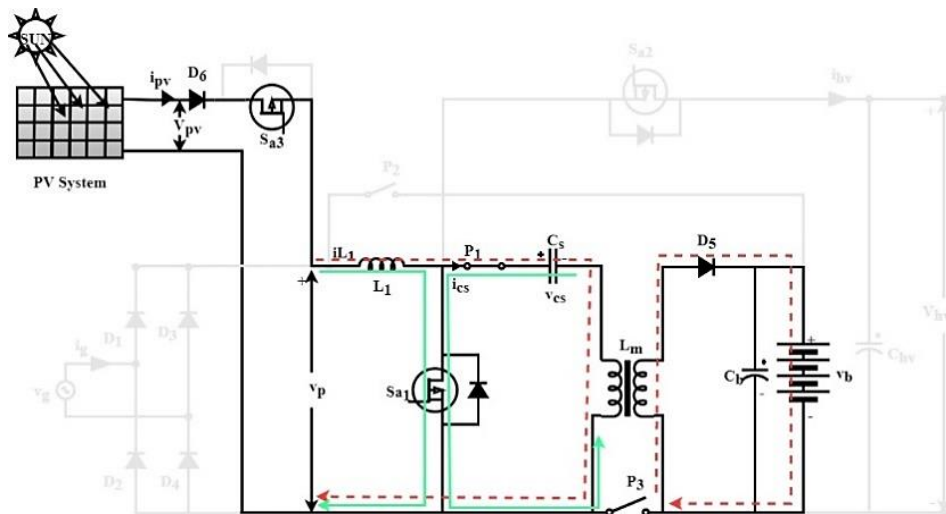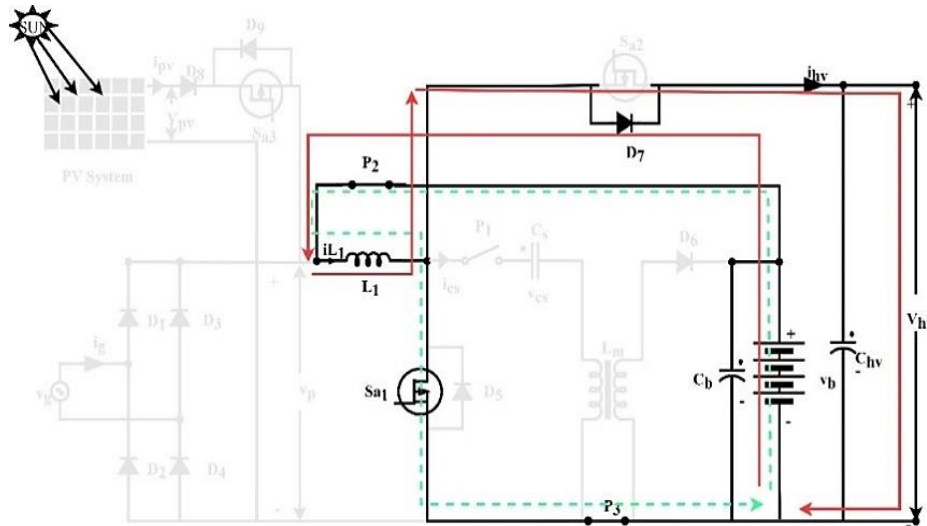Figure 6. Equivalent circuit of the proposed converter - Mode 1

Figure 7. Equivalent circuit of the proposed converter - Mode 2

- Mode 3: Propulsion mode

The battery discharges to the DC-link capacitor in this setup. The P2 and P3 are ON. Inductor L1 is charged when S_{a1} is ON. When S_{a1} is turned -OFF, inductor L1 supplies to C_{hv} and supplies to load. The current flow is depicted with solid lines. Figure 8 depicts the equivalent circuit of this mode.

- Mode 4: Regenerative braking

In this, regenerative braking is applied, and the motor winding stored energy is used to recharge the battery. The battery receives the energy that is stored in the DC link. This results in an improvement in the run time of the vehicle. In this, P2 and P3 are ON, and S_{a2} is ON. The motor load charges the L1, and Figure 9 depicts the current's path through L1 as a dotted line and when S_{a2} is OFF, L1 is discharged and supplies the battery. Figure 9 depicts the current's path through L1 as a solid line.

Figure 8. Equivalent circuit of the proposed converter - Mode 3
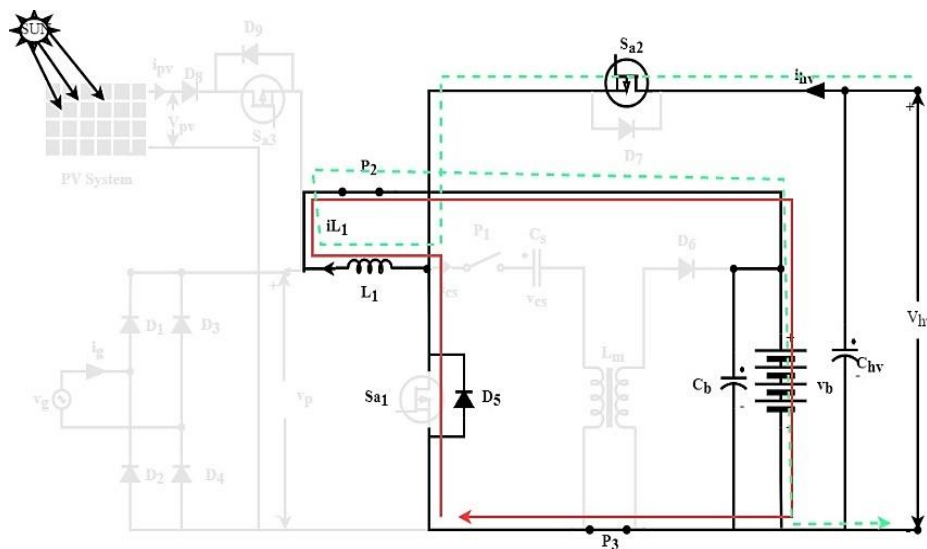
Figure 9. Equivalent circuit of the proposed converter - Mode 4

3. DESIGN PROCEDURE OF THE PROPOSED CONVERTER

The proposed converter parameters are designed as per the following equations. There are elements utilized only for one mode, and there are also a few elements used in multiple modes. Hence the design includes all the modes, and a suitable value is assigned to the circuit components.

3.1. Mode 1

In this state, the battery is supplied by the capacitor C_b. When the S_{a1} is switched ON, the inductors L_1 and L_m get charged. The L_m and L_1 get discharged, C_s get charged, and the power to the load is provided when S_{a1} is OFF. Following is the inductor value for this mode.

$$L_1 = \frac{V_s * d_1}{\Delta I_{L1} * F_s} \tag{6}$$

The inductor ripple current is provided in (7). In addition, the expressions for d_1 and L_1 is also provided as follows:

$$\Delta i_{L1} = \aleph\% i_s \tag{7}$$

$$d_1 = \frac{V_b}{V_s + V_b} \tag{8}$$

$$L_1 = \frac{V_s^2 * d_1}{P_s * F_s * \aleph} \tag{9}$$

substituting d_1 in (9), the inductor is calculated as (10).

$$L_1 = \frac{V_s^2}{P_s * F_s * \aleph} * \frac{V_b}{V_b + V_s} \tag{10}$$

Where $i_s = (\frac{P_S}{V_s})$, V_s is grid voltage, P_s is power flow on the grid side, d_1 is the pulse width of S_{a1}, and F_s is switching frequency, correspondingly. The L_m is provided in (11).

$$L_m = V_b \frac{1 - d_1}{\Delta I_{Lm} * F_s} \tag{11}$$

Substituting d_1 in (11), the magnetic inductance is given as (12).

$$L_m = \frac{V_s^2}{P_s * F_s * \pi\%} * \frac{V_b}{V_b + V_s} \tag{12}$$

Where Δi_{Lm} is $\pi\%$ of i_s and $i_s = \left(\frac{P_S}{V_s}\right)$. The expression for the C_s with k% of ripple voltage in V_{Cs} is presented in (13).

$$C_s = V_b \frac{d_1(t)}{k V_c(t) * F_s R_L} \tag{13}$$

Where V_c is capacitor voltage. The d_1 and $V_c(t) = |V_s(t)|$ and $R_L = V^2_b/P_b$, are substituted in (13). Therefore, the inductance is calculated using (14).

$$L_1 = \frac{V_s^2}{k * |V_s(t)| * F_s * \frac{V_b^2}{P_b}} * \frac{V_b}{V_b + V_s} = \frac{P_b}{k * |V_s(t)| * F_s * (V_b + V)_s} \tag{14}$$

The $V_{s,\,max}$ and V_b are considered for the calculation of C_s. The C_b is designed in order to minimize the second-order harmonic (100 Hz) ripples across C_b. Hence, the C_b is provided in (15).

$$C_b = \frac{I_b}{2\omega \Delta V_{Cb}} = \frac{\frac{P_b}{V_b}}{2\omega \delta\% V_b} = \frac{P_b}{2\omega \delta\% V_b^2} \tag{15}$$

Where ΔV_{cb} is $\delta\% V_b$, $\omega = 2\pi f_L$ and f_L is supply frequency.

3.2. Mode 2

In this, the switch S_{a3} is turned on, and the battery is charged using power from the PV system. The L_1 is made similar to mode 1 and is as (16).

$$L_1 = \frac{V_{pv} - d_2}{\Delta I_{L1} * F_s} \tag{16}$$

Where $\Delta I_{L1,\,PV} = \xi\% I_{pv}$. The d_2 is provided in (17).

$$d_2 = \frac{V_b}{V_{PV}+V_b} \tag{17}$$

Placing the d_2 in inductance, the expression for L_1 is as (18).

$$L_1 = \frac{V_{PV}{}^2}{P_{PV}*F_s*\varepsilon\%} * \frac{V_b}{V_b+V_{PV}} \tag{18}$$

Where P$_{PV}$ and V$_{PV}$ are the PV power and voltage, respectively. The value of L_m is calculated using (19).

$$L_m = V_b \frac{1-d_2}{\Delta I_{Lm}*F_s} \tag{19}$$

Substituting d_2 in (19), the L_m is calculated as (20).

$$L_m = \frac{V_{PV}{}^2}{P_{PV}*F_s*\gamma\%} * \frac{V_b}{V_{mp}+V_{PV}} \tag{20}$$

Where $\Delta i L_m$ is γ% of I$_{pv}$ and I$_{pv}$=(P$_{PV}$/V$_{PV}$).

3.3. Mode 3

In this mode, inductor L_1 is charged when S$_{a1}$ is ON, and when S$_{a1}$ is turned -OFF, inductor L_1 supplies to C$_{hv}$ and supplies to load. The L_1 in mode 3 is designed as provided in (21).

$$L_1 = \frac{V_b*d_3*T_s}{\Delta I_{L1}} \tag{21}$$

Substituting F$_s$=1/T$_s$, the L_1 is rewritten as (22).

$$L_1 = \frac{V_b*d_3}{\Delta I_{L1}*F_s} \tag{22}$$

Where ΔI_{L1} is η% i$_b$ and $d_3 = 1 - V_b/V_{hv}$. The C_{hv} is designed as (23).

$$C_{hv} = \frac{d_3}{R_L*F_s*\frac{\Delta V_{hv}}{V_{hv}}} \tag{23}$$

Where ΔV_{hv} is capacitor ripple voltage, $d_3 = 1 - V_b/V_{hv}$, and R_L= V^2$_{hv}$/P$_{hv.}$

3.4. Mode 4

In this, S$_{a2}$ is ON. The L_1 is charged by motor load, and when S$_{a2}$ is OFF, L_1 is discharged and supplies the battery. The L$_{1, RB}$ in mode 4 is designed and provided as (24).

$$L_1 = \frac{(\Delta V_{hv}-V_b)*d_4}{\Delta I_{L1}*F_s} \tag{24}$$

Substituting V_b in (24), the L_1 is rewritten as (25).

$$L_1 = \frac{(\Delta V_{hv}-d_4 V_{hv})*d_4}{\Delta I_{L1}*F_s} = \frac{(1-d_4)*V_{hv}d_4}{\Delta I_{L1}*F_s} \tag{25}$$

Where ΔI_{L1}= μ% i$_{hv}$ and d_4= V$_b$/V$_{hv}$.

4. PROPOSED MAXIMUM POWER POINT TRACKING TECHNIQUE

This section discusses the traditional P&O and INC MPPT techniques. In addition, this section also discusses the proposed modified P&O algorithm for MPPT applications.

4.1. Proposed P&O algorithm

The P&O algorithm is used to track and extract the maximum power from the PV system. In this algorithm, the PV voltage is perturbed little, and the (ΔP) is measured. If ΔP is positive, then the perturbation of the PV voltage reaches closer to MPP. Thus, the perturbations continue until ΔP stays in a positive zone, as presented in (26). If ΔP is negative, then the perturbation of the PV voltage is moving farther to MPP, and the direction of the perturbation is to be reversed so that the power reaches MPP [37]. The P&O algorithm-based MPPT is provided in Figure 10.

$$\left. \begin{array}{l} \text{If} \frac{\Delta P}{\Delta V} > 0, \Delta D \text{ is positive} \\ \text{If} \frac{\Delta P}{\Delta V} < 0, \Delta D \text{ is negative} \end{array} \right\} \qquad (26)$$
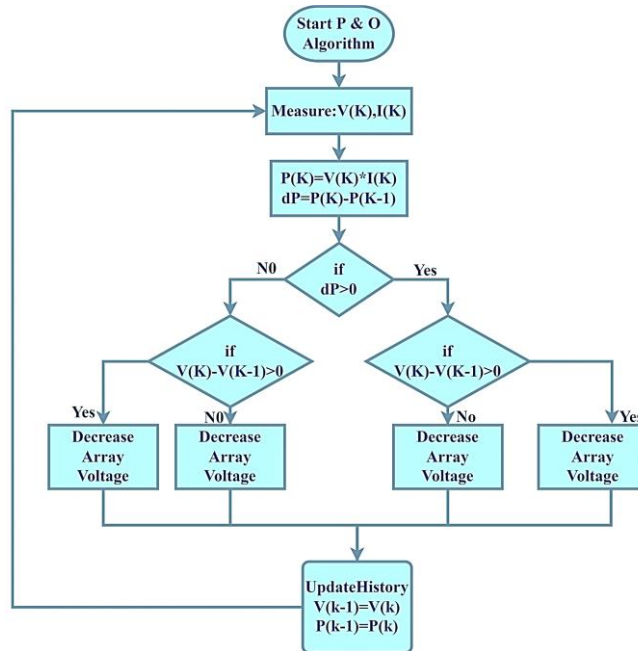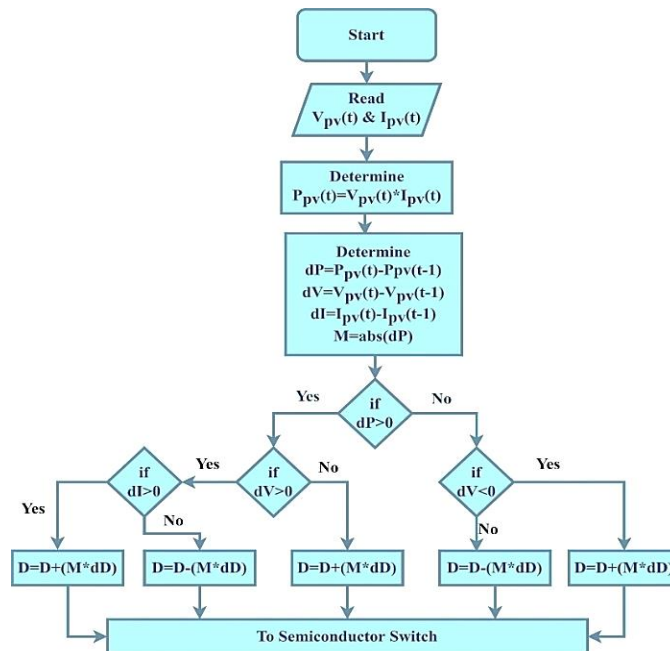
Figure 10. Flowchart for P&O algorithm based MPPT

Figure 11. Flowchart for modified P&O algorithm-based MPPT

Since the variables dI and dV seem to be positive, its additional variable, dI, can detect an increase in solar irradiance. In order to avoid the drift problem, the duty ratio is modified to decrease the operating voltage, where dV and dI are positive. This is done by moving the switching point closer to the MPP.

Figure 11 shows the flowchart for the modified P&O-based MPPT technique. As shown in the flowchart for the adaptive P&O (AMP&O) algorithm, the scaling factor, *M*, alters the perturbation size, as presented in (27).

$$M = \frac{[V_{pv}(t+1)-V_{pv}(t)]}{[P_{pv}(t+1)-P_{pv}(t)]} \times \frac{[P_{pv}(t)-P_{pv}(t-1)]}{[V_{pv}(t)-V_{pv}(t-1)]} = \frac{\Delta V_{pv}}{\Delta P_{pv}} \times \frac{dP_{pv}}{dV_{PV}} \tag{27}$$

In a start-up, the variable M must be tuned appropriately to perform better under all conditions. Initially, the dP/dV is maximum, but due to lower values of ΔV/ΔP, the dP/dV is also reduced. Hence the performance is better in steady-state conditions. The performance is better in transient conditions due to automated M tuning than manual tuning or fixed value.

4.2. Incremental conductance (INC) method

This method assumes that a change in output conductance ratio is equivalent to a negative output conductance ratio. The peak PV power for this technique is over 98% of its incremental conductance. Figure 12 shows the flowchart for implementing the INC algorithm. The INC algorithm determines the P-V curve's slope, and the maximum power point is traced by looking for the P-V curve's peak. The INC algorithm employs the instantaneous conductance I/V and the incremental conductance dI/dV. In 28 is used in the traditional incremental conductance algorithm to find the MPP, and the MPPT controller measures the PV module's voltage and current.
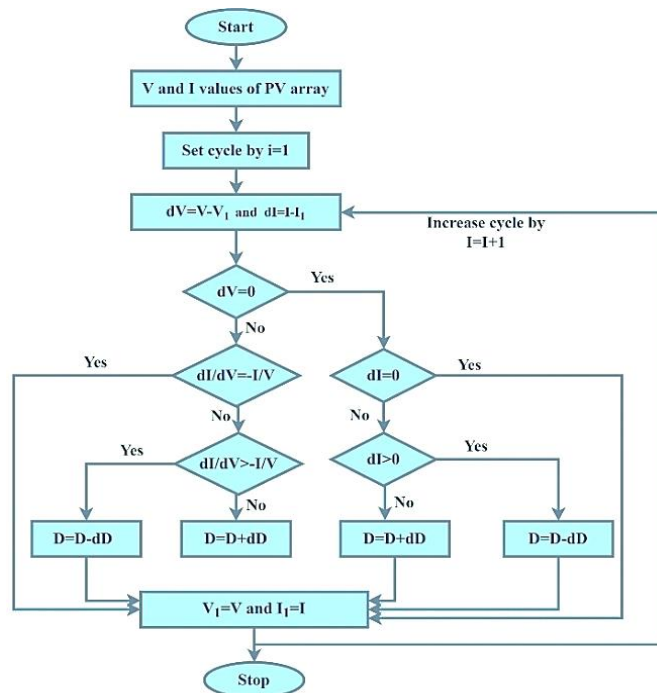
$$I + V\frac{d_i}{d_v} = 0 \tag{28}$$

Figure 12. Flowchart for INC-based MPPT

5. PROPOSED CONTROL STRATEGY

In mode 1, the traditional proportional integral (PI) controller is utilized, and the maximum power point tracking controller is utilized in mode 2. PI controllers are used in two loops for modes 2 and 4. When the voltage at the source is equal to the inductor voltage, S_{a1} is turned OFF by a flip flop that has been set by a clock or gating pulse. In mode 3, the output voltage is regulated in order to keep it constant under any conditions so that the vehicle operation is smooth. In mode 3, the PI controller is given the difference in voltage between the reference voltage and the measured voltage, and it generates the reference battery current, which is compared with the measured battery current, and the error is provided to the inner PI controller. The inner PI controller generated the duty ratio and subjected it to PWM, and the pulses were provided to S_{a1}. The control structure for modes 1 and 2 is shown in Figure 13, and for modes 3 and 4 is shown in Figure 14.
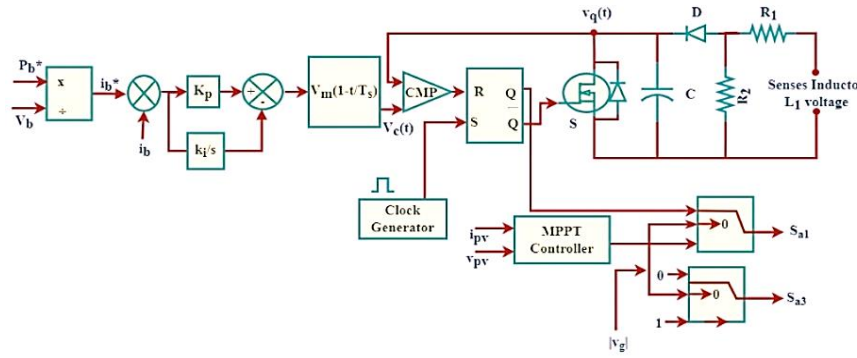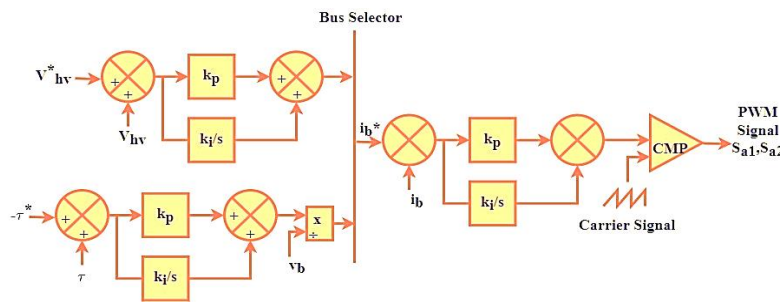
Figure 13. Control structure for modes 1 and 2

Figure 14. Control structure for modes 3 and 4

6. RESULTS AND DISCUSSIONS

This section analyses the simulation and hardware results obtained for different MPPT algorithms.

6.1. Simulation results

The entire system has been modelled in the MATLAB/Simulink software suite and evaluated for various operational scenarios, as was previously stated. In mode 1, the SEPIC converter receives a 150 V supply voltage between t=0 and t=0.5 s. Next, the source is interrupted, and from t=0.5 to t=2 s, PV serves as the source. These two possibilities both involve charging the battery, and the motor will be in a standstill condition. At t=2 s (mode 3), the motor starts to operate in the forward direction, and the battery starts to discharge. At t=3.5 s (mode 4), the regenerative braking is applied to the motor, and the charge present in the motor windings is retrieved to charge the battery.

6.1.1. Mode 1: Grid charging mode

Figure 15 shows the voltage and current waveforms of the grid. Grid voltage and current peak levels are roughly 210 V and 20 A, respectively. The zero-phase transition between the voltage across the grid and the current causes the boost in power factor. Figures 16 and 17 depict the voltage and current waveforms of the battery while they are being charged by the grid. In this, the current is roughly 25 A, while the battery voltage remains at 52 V (which is greater than the 48 V standard battery voltage). Figure 18 depicts the voltage waveform across the capacitor C_s. Figure 19 depicts the voltage across switch S_{a1}. PV supplies battery energy while the grid is cut off at t=0.5 s.
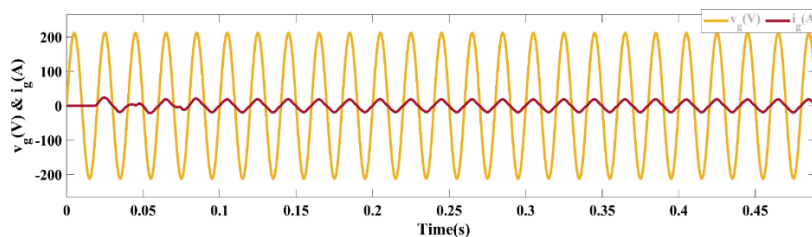

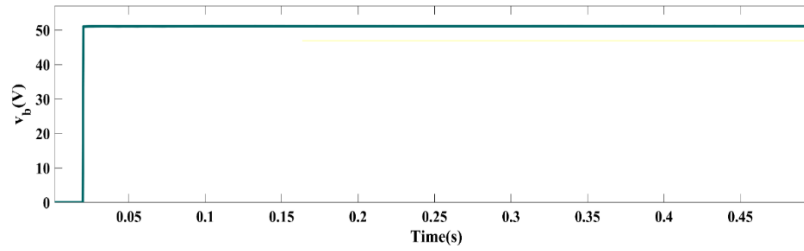Figure 15. Current and voltage waveforms of the grid
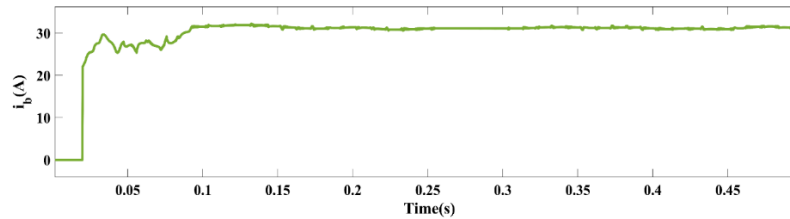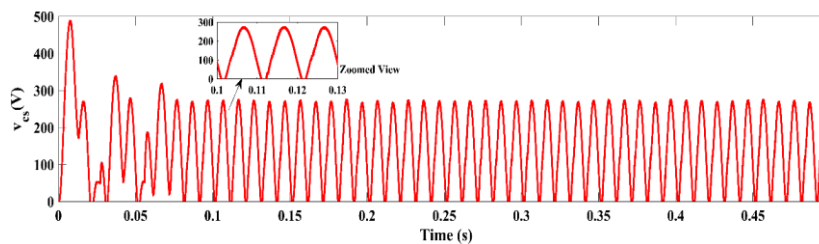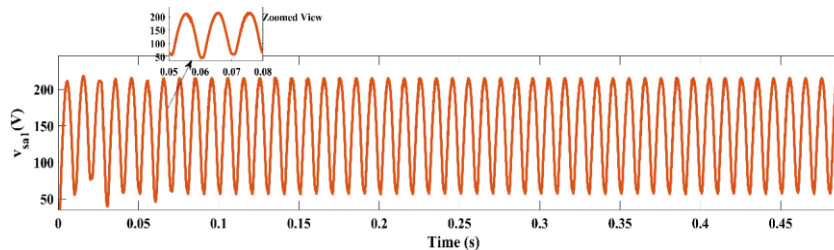
Figure 16. Mode 1 - Battery voltage

Figure 17. Battery current waveform in mode 1

Figure 18. Capacitor (C_s) voltage waveform

Figure 19. Switch (S_{a1}) voltage waveform

6.1.2. Mode 2: PV charging mode

The battery current is roughly 25 A, and the battery voltage remains stable at 52 V (which is greater than the standard battery value of 48 V). At t=0.5 s, the grid is cut off, and PV powers the battery charge. Figure 20 provides the irradiation for the production of photovoltaic power. Between t=0.5 s and t=1, the sun irradiation is around 500 W/m², between t=1 s and 1.5 s, it is 1000 W/m², and between t=1.5 s and 2 s, it is lowered to 500 W/m².

Irradiation is brought down to zero after a period of two seconds. Figure 21 depicts the photovoltaic electricity produced as a result of the solar irradiation discussed earlier. The photovoltaic power produced between t=0.5 s and 1 s is approximately 406 W, while between t=1 s and 1.5 s, the amount of power produced is approximately 809 W (97.94%). Between t=1.5 s and 2 s, the photovoltaic output is 406 W (98.3%); between t=1.5 s and 2 s, the photovoltaic output is 406 W (98.3%). The incremental conductance algorithm replaces the P&O algorithm, and the same irradiation levels are applied to the PV array. The PV power with incremental conductance algorithm is provided below in Figure 22. In this, the photovoltaic power produced between t=0.5 s and 1 s is about 409 W, between t=1 s and 1.5 s, the photovoltaic output produced is about 809 W (97.94%), and between t=1.5 s and 2 s, the output of the photovoltaic source is 409 W (99.03%). The Modified P&O

algorithm replaces the incremental conductance algorithm, and the same irradiation levels are applied to the PV array. The PV power with the modified P&O algorithm is provided below in Figure 23. In this, the power produced between t=0.5 s and 1 s is about 412 W, between t=1 s to 1.5 s, the output of the PV is about 809 W (97.94%), and between t=1.5 s and 2 s, the output of the photovoltaic source is 412 W (99.76%). Here, the modified P&O algorithm extracts PV power slightly higher than the incremental conductance algorithm under shaded conditions, whereas both algorithms extract the same power without shading. The modified P&O algorithm extracts more power than conventional P&O and incremental conductance algorithms under shaded conditions, and under unshaded conditions, all three algorithms extract the same power. The battery current and voltage during mode 2 are illustrated in Figures 24 and 25.
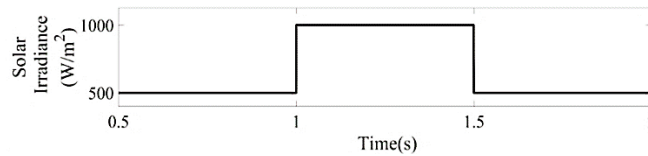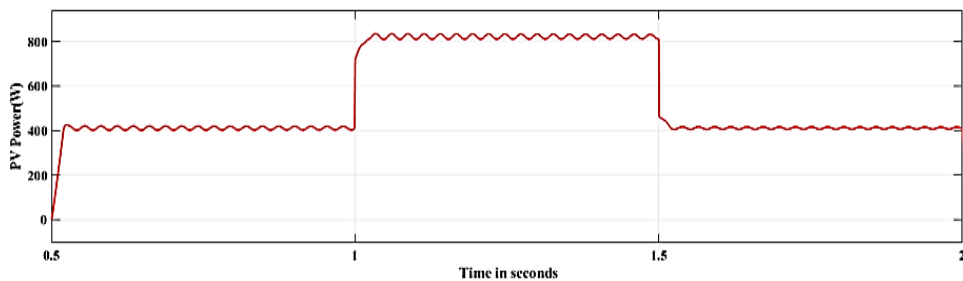
Figure 20. Shading pattern

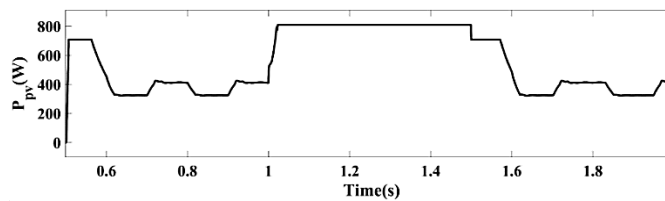Figure 21. PV power in mode 2 with conventional P&O algorithm

Figure 22. Output power of the PV in mode 2 obtained by the INC algorithm
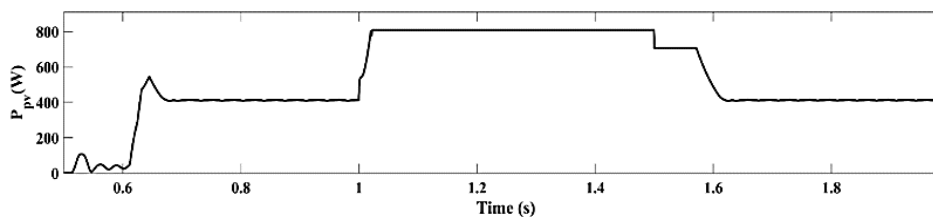
Figure 23. Output power of the PV in mode 2 obtained by the modified P&O algorithm
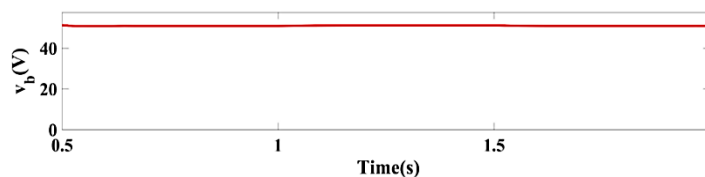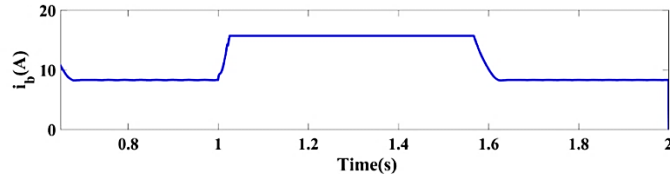
Figure 24. Mode 2 - Battery voltage

Figure 25. Battery current waveform in mode 2

The current flow at these timings only provides that the PV functions in mode 2. Even without voltage from the supply, it charges the battery. The current at the battery is about 10 A from t=0.5 s to t=1 s, and between t=1 s and 1.5 s, the current is 15.6 A, and between t=1.5 s and 2 s, irradiance is minimized toward 10 A. After t=2 s, the PV is disconnected, and the vehicle starts to operate in forward mode (mode 3). Table 1 shows the power extracted by modified P&O for different solar irradiations. Table 2 shows the comparison of MPPT algorithms.

Table 1. Power extracted by modified P&O

Solar irradiation (W/m2)	Rated PV power (W)	Power extracted by MP&O (W)	Efficiency (%)
1000	826	809	97.94
800	660.8	657	99.42
500	413	412	99.76
200	165.2	87.3	52.8

Table 2. Comparison of MPPT algorithms

MPPT Algorithms	Irradiation–1000 W/m^2			Irradiation–500 W/m^2		
	Rated PV Power (W)	Power extracted by MPPT (W)	Efficiency (%)	Rated PV Power (W)	Power extracted by MPPT (W)	Efficiency (%)
P&O	826	809	97.94	413	406	98.3
INC	826	809	97.94	413	409	99.03
Improved P&O	826	809	97.94	413	412	99.76

6.1.3. Mode 3: Propulsion mode

In this mode, the vehicle is accelerated by charging the DC-link capacitor with the energy that was previously stored within the battery throughout PIN charging and RBG modes. In mode 3, the voltage and current of the battery are depicted in Figures 26 and 27, respectively. In this mode, the load increases at t=2.5 s and is reduced at t=3 s. The current at the battery is about 10 A between t=2 s and t=2.5 s, and between t=2.5 s and 3 s, the current is 15.6 A, and between t=3 s and 3.5 s, the current is reduced to 10 A. After t=3.5 s, the regenerative braking is applied to the vehicle, and the battery acquires the energy that is stored in the motor windings. The motor voltage and current are provided below in Figures 28 and 29.
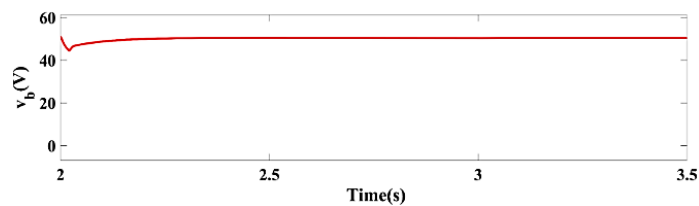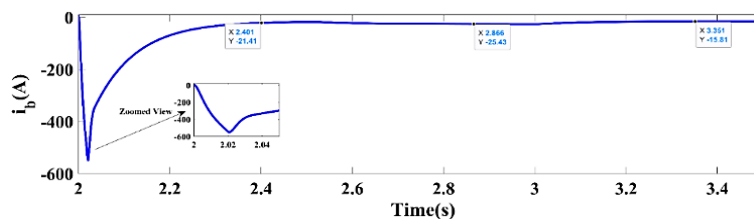

Figure 26. Battery voltage waveform in mode 3

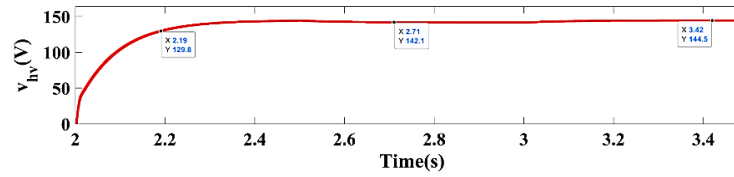Figure 27. Battery current waveform in mode 3
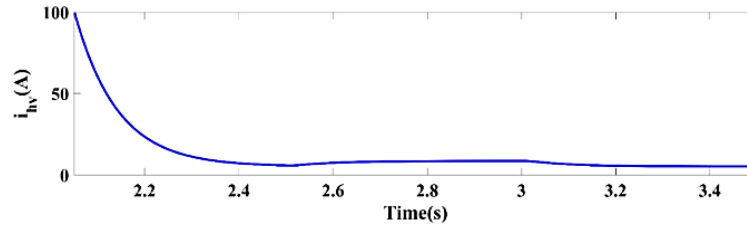
Figure 28. Motor voltage waveform in mode 3

Figure 29. Motor current waveform in mode 3

6.1.4. Mode 4: Regenerative braking

In this, regenerative braking is applied, and the motor windings' stored energy is used to recharge the battery. The battery receives the energy that is stored in the DC link. At t=3.5 s, the regenerative braking is applied, and the current flow is in a negative direction, i.e. it is fed back to the battery to charge it. The battery voltage battery current is provided below in Figure 30, Figure 31 and the motor voltage in Figure 32. The battery is initially charged by source and PV until t=2 s; hence, the battery voltage is high, and SOC increases. As the motor starts at t=2 s, the SOC starts to reduce due to discharging of the battery. At t=3.5 s, the regenerative braking is applied; hence, the battery is again charged and %SOC and voltage increase. The SOC (%) is shown in Figure 33.
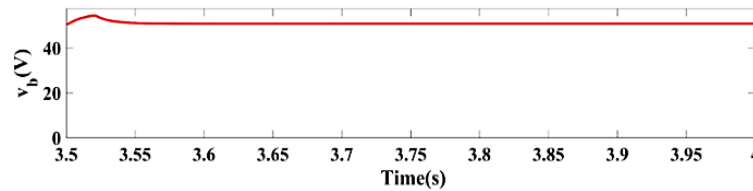

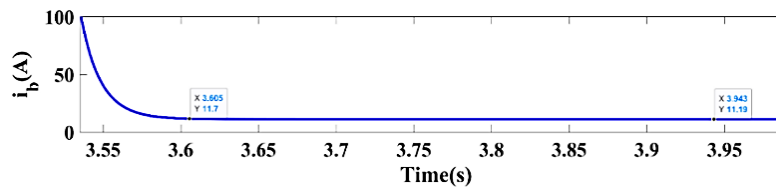Figure 30. Battery voltage waveform in mode 4
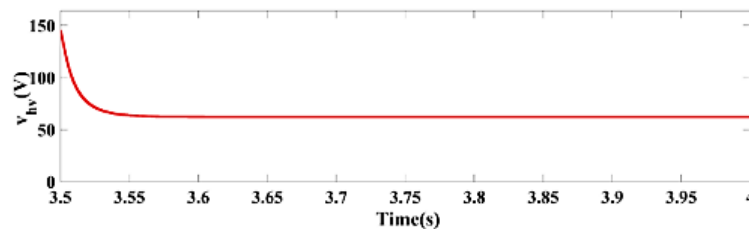

Figure 31. Battery current waveform in mode 4

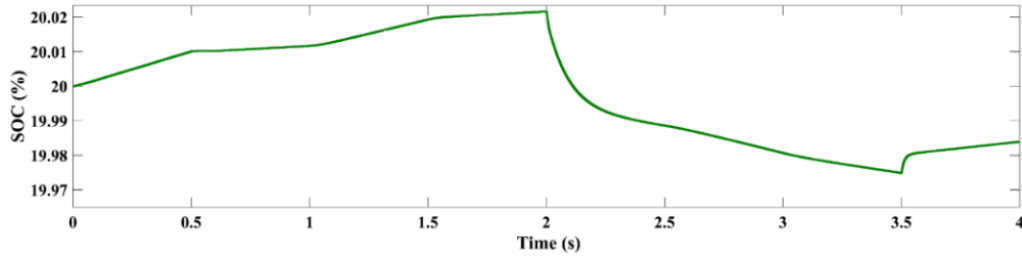Figure 32. Motor voltage waveform in mode 4

Figure 33. State of charge (%)

6.2. Hardware results

The hardware block diagram of the proposed converter is shown in Figure 34. In order to convert the voltage ratio to 230/12 V, 1 A, 50 Hz and regulate the DC voltage, a single-phase AC supply of 230 V, 50 Hz, is used to power the step-down transformer. A diode rectifier transforms the 12 V AC voltage to 12 V DC voltage. The rectified DC voltage is provided to 5 V and 12 V Voltage regulators. The Arduino microcontroller receives the regulated voltage of 5 V, and the microcontroller produces the pulses in accordance with the control scheme. The gate pulses that are produced by the controller are matched up with the 12 V regulated supply that is delivered to the driver circuit. This allows the driver circuit to remain capable of operating the power electronic switches that are a part of the proposed converter. In this, a single-phase AC supply of 230 V, 50 Hz, is provided as a supply for the control circuit, which consists of the microprocessor to generate the pulses and a driver circuit which drives the gate of power electronic switches using the pulses generated from the processor. A step-down transformer is used. By using this, the 230 V AC main supply is stepped down to 12/24 V AC is given to the rectifier, which converts the AC supply to a DC supply. Basically, rectifiers convert AC to DC. From the step-down transformer, a supply of 12 V AC is given to the rectifier, which converts AC to DC supply. In the end, we get a 12 V DC supply. A voltage regulator is used to maintain a constant voltage level. Two voltage regulators provide 5 V and 12 V DC supply from 12 V AC supply, i.e. 5 V for the buffer IC and 12 V for the driver circuit. A buffer is a circuit that produces the same voltage output that is input into it. The high input impedance allows the full voltage to fall across the buffer. It is used between the controller and the driver circuit. The specifications of the components are listed in Table 3.
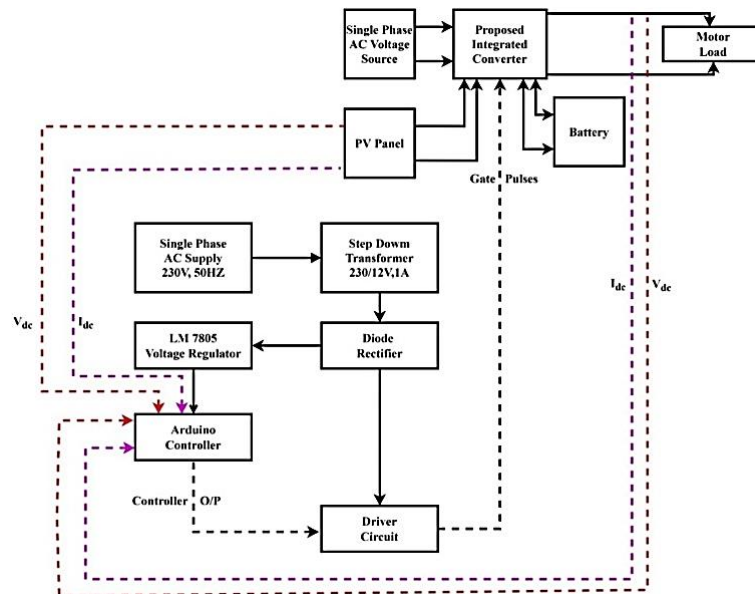

Figure 34. Block diagram of proposed converter

The experimental prototype is shown in Figure 35. The pulse generated is provided to the buffer IC (CD 4050), which provides isolation between the controller and the other driver circuit components. The supply of driver IC is provided by a step-down transformer (230-12 V), which is rectified and provided to V_{cc}

and ground ports. The output of the driver IC is provided to the power electronic switches according to the modes. In Figure 36, the supply voltage is around 48 V and 2 A. The supply can be used to charge the battery, and the waveforms of the source voltage can be provided.

Table 3. Hardware specifications

| Components name	Components range	Components quantity	Components name	Components range	Components quantity
U1560-Diodes	200 V, 15 A	3	Battery (Lead Acid)	12 V, 7.5 Ah	3
	1000 µF, 25 V	3	TLP 250 - Driver IC	12 V, 1.5 A	3
Capacitors (Electrolytic)	220 µF, 100 V	1	CD 4050 Buffer IC	3-18 V, 0.32 mA	1
	1000 µF, 200 V	2	Regulator, 7812	12 V, 1 A	1
	1000 µF, 100 V	1	Regulator, 7805	5 V, 1 A	1
Transformer (Step-down)	12 V, 750 mA	1	1N4007 - Diode	700 V, 1 A	3
	48 V, 2 A	1	Arduino UNO Controller	7-12 V, 20 mA	1
Bridge Rectifier, BR1010	700 V, 10 A	1	IRF250N - MOSFET	200 V, 30 A	3
Bridge Rectifier, W04M	400 V, 1 A	2			
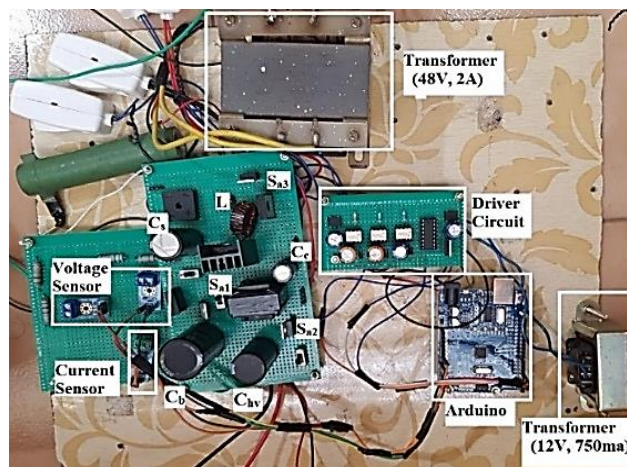
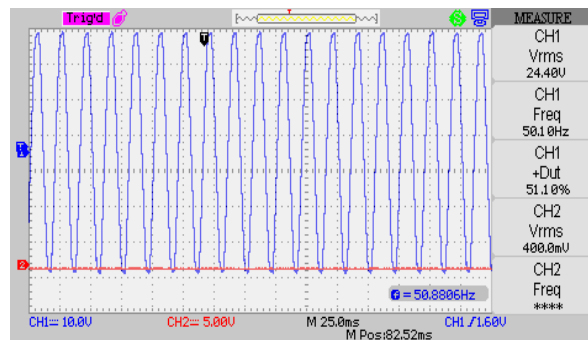Figure 35. Experimental setup of the proposed system

Figure 36. Source voltage waveform

In this, the source voltage of 48 V is applied to the proposed SEPIC converter as AC supply. Then the supply is tripped, and the DC supply (PV) of 12 V, 1 A is connected as the source. During these two modes, the P1 manual switch is ON while P2, P3, and P4 are OFF, the battery (3*12 V, 7.5 Ah) is charging, and the HV (High Voltage) DC load is still in the open circuit. In mode 3, the HV DC load is connected as P1 is OFF and P2, P3, and P4 are ON, and the battery starts discharging. The voltage sensor and current sensor first detect PV voltage, PV current, and load voltage. Sensed values are provided to the Arduino, where the pulses are generated according to the operational modes. When AC supply is available, S_{a3} is ON, and S_{a1} operates at high frequency for the boost and buck operations. The current limiting resistors reduce the current flow in both the input and battery sides. The sensor is of lower ratings; hence, the potential divider or voltage divider reduces the voltage value measured by the sensor, and the actual values are calculated with Arduino for control loops.

In Figure 37, the supply voltage is measured as 24.4 V of 50 HZ frequency after the current limiting resistor in which there was an occurrence of voltage drop and the rectified DC voltage is provided in Figure 37. In Figure 38, we get the dc voltage of 32.8 V as the RMS value, the efficiency of the bridge rectifier is around 71.3%, and the maximum efficiency is claimed to be 81.2%. The switch (S_{a1}) voltage is provided when the PV source is connected.

The battery voltage before and after the charging is provided in Figure 39, The voltage of the battery before the charging starts is around 34.4 V, and when the charging occurs, it is increased to 35.2 V. The inductor voltage is shown in Figure 40, and the inductor voltage is positive while it is charging, negative while it is discharging, and the overall inductor voltage is around 18 V, around 55% of the input DC voltage. The coupling capacitor voltage of the converter is shown in Figure 41. Similar to the inductor, the capacitor voltage increases gradually from positive while charging and negative while discharging. The overall voltage is around 10.4 V, which is around 58% of the inductor voltage and 32% of the input DC link voltage. The high voltage load voltage of the suggested SEPIC converter in mode 3 operation is provided. In Figure 42, the RMS voltage is around 87.2 V, and the DC link voltage is around 123 V when mode 3 starts operating. The battery starts to discharge as it acts as the supply.
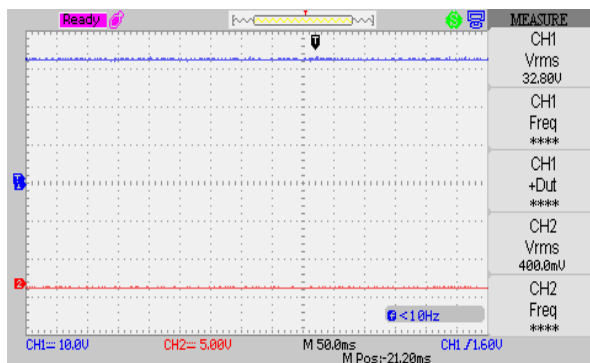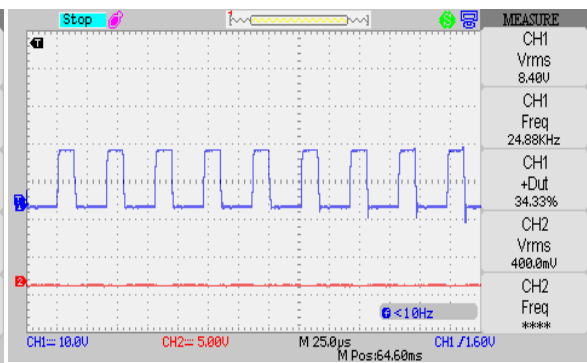

Figure 37. Rectified DC voltage waveform

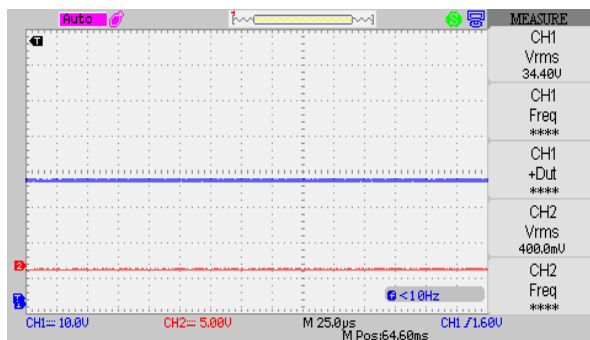Figure 38. Switch S_{a1} voltage waveform

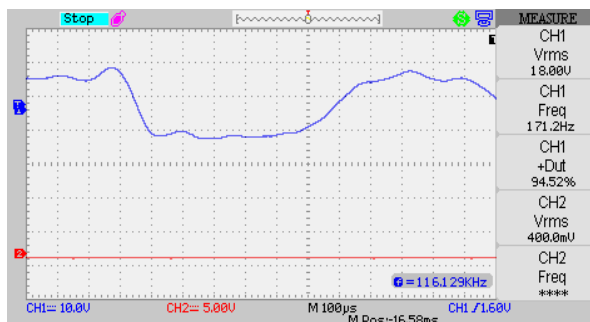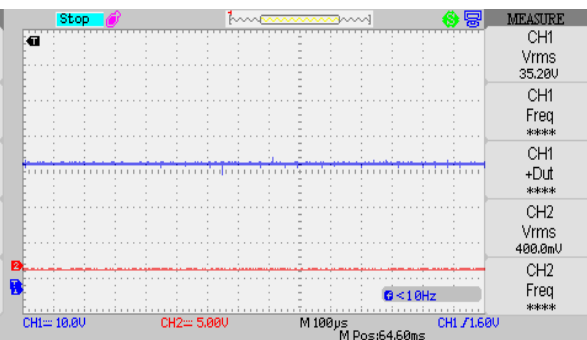Figure 39. Battery voltage before and after the charging
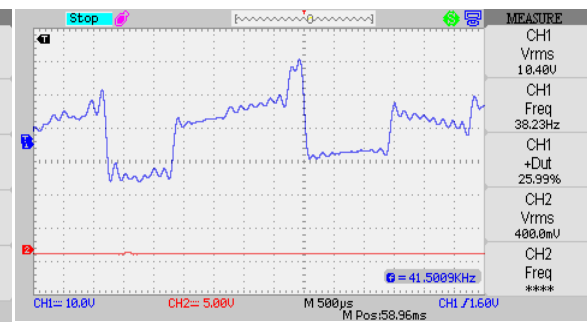

Figure 40. Inductor voltage waveform

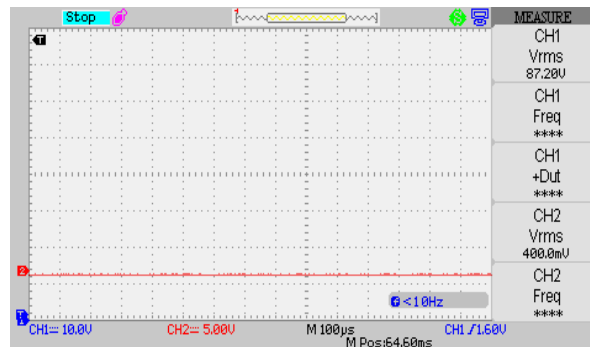Figure 41. Coupling capacitor voltage waveform

Figure 42. RMS voltage waveform

7. CONCLUSIONS

This article presents the design and analysis of a SEPIC converter intended for use in battery charging applications as well as for electric vehicle purposes. The operational modes are controlled by a controller configuration based on the load requirements and PV power generation. The fluctuation in current (dI), in addition to voltage and power conditional statements, is recommended to be incorporated into the MPPT algorithm to create an improved P&O algorithm-based MPPT. The suggested methodology is simulated, and the suggested method's efficacy is verified with fixed and variable irradiations. Regenerative braking is applied as the energy stored in motor windings is retrieved to charge the battery and increase the run time of the vehicle. The modified P&O algorithm replaces the incremental conductance and P&O algorithms. Because the modified P&O algorithm extracts PV power slightly higher than the incremental conductance algorithm under shaded conditions, whereas both algorithms extract the same power without shading. The modified P&O algorithm extracts more power than conventional P&O and incremental conductance algorithms under shaded conditions, and under unshaded conditions, all three algorithms extract the same power. Finally, based on the findings, it is proved that the suggested PV system for EV battery charging application is effective and efficient.

Though the performance of the proposed converter strategy delivers competitive results, it is essential to validate the performance in a real-time environment. The application of the proposed charging strategy can be extended to other distributed energy sources. The converter voltage gain and efficiency can be improved by employing boosting techniques, such as voltage multipliers, voltage doublers, coupled inductors, and transformers. It is also proposed to the extent of MPPT by employing metaheuristic optimization-based MPPT techniques.

REFERENCES

[1] J. C. D. Mushini, K. Rana, and M. S. Aspalli, "Analysis of open circuit voltage and state of charge of high power lithium ion battery," *International Journal of Power Electronics and Drive Systems*, vol. 13, no. 2, pp. 657–664, Jun. 2022, doi: 10.11591/ijpeds.v13.i2.pp657-664.

[2] X. Wang *et al.*, "Effects of Different Charging Currents and Temperatures on the Voltage Plateau Behavior of Li-Ion Batteries," *Batteries*, vol. 9, no. 1, p. 42, Jan. 2023, doi: 10.3390/batteries9010042.

[3] P. Makeen, H. A. Ghali, and S. Memon, "Investigating an influence of temperature and relative humidity on the electrical performance of lithium polymer ion battery using constant-current and constant voltage protocol at small scale for electric vehicles," in *11th International Conference on Power Electronics, Machines and Drives (PEMD 2022)*, 2022, pp. 126–130, doi: 10.1049/icp.2022.1030.

[4] Y. Miao, P. Hynan, A. Von Jouanne, and A. Yokochi, "Current li-ion battery technologies in electric vehicles and opportunities for advancements," *Energies*, vol. 12, no. 6, p. 1074, Mar. 2019, doi: 10.3390/en12061074.

[5] K. Chen, F. Zhao, H. Hao, and Z. Liu, "Selection of lithium-ion battery technologies for electric vehicles under China's new energy vehicle credit regulation," *Energy Procedia*, vol. 158, pp. 3038–3044, Feb. 2019, doi: 10.1016/j.egypro.2019.01.987.

[6] V. Ruiz, "Standards for the Performance and Durability Assessment of Electric Vehicle Batteries," 2018. [Online]. Available: https://www.apren.pt/contents/publicationsothers/ec-standards-for-the-performance-and-durability-assessment-of-ev-batteries.pdf.

[7] A. K. Mishra and B. Singh, "Control of SRM drive for photovoltaic powered water pumping system," *IET Electric Power Applications*, vol. 11, no. 6, pp. 1055–1066, Jul. 2017, doi: 10.1049/iet-epa.2016.0303.

[8] H. M. El-Helw, A. Magdy, and M. I. Marei, "A Hybrid Maximum Power Point Tracking Technique for Partially Shaded Photovoltaic Arrays," *IEEE Access*, vol. 5, pp. 11900–11908, 2017, doi: 10.1109/ACCESS.2017.2717540.

[9] M. Kermadi, Z. Salam, J. Ahmed, and E. M. Berkouk, "An Effective Hybrid Maximum Power Point Tracker of Photovoltaic Arrays for Complex Partial Shading Conditions," *IEEE Transactions on Industrial Electronics*, vol. 66, no. 9, pp. 6990–7000, Sep. 2019, doi: 10.1109/TIE.2018.2877202.

[10] G. R. C. Mouli, P. Bauer, T. Wijekoon, A. Panosyan, and E. M. Bärthlein, "Design of a power-electronic-assisted OLTC for grid voltage regulation," *IEEE Transactions on Power Delivery*, vol. 30, no. 3, pp. 1086–1095, Jun. 2015, doi: 10.1109/TPWRD.2014.2371539.

[11] G. R. C. Mouli, J. Schijffelen, M. Van Den Heuvel, M. Kardolus, and P. Bauer, "A 10 kW Solar-Powered Bidirectional EV Charger Compatible with Chademo and COMBO," *IEEE Transactions on Power Electronics*, vol. 34, no. 2, pp. 1082–1098, Feb. 2019, doi: 10.1109/TPEL.2018.2829211.

[12] S. M. Shariff, M. S. Alam, F. Ahmad, Y. Rafat, M. S. J. Asghar, and S. Khan, "System Design and Realization of a Solar-Powered Electric Vehicle Charging Station," *IEEE Systems Journal*, vol. 14, no. 2, pp. 2748–2758, Jun. 2020, doi: 10.1109/JSYST.2019.2931880.

[13] A. Khan, S. Memon, and T. P. Sattar, "Analyzing Integrated Renewable Energy and Smart-Grid Systems to Improve Voltage Quality and Harmonic Distortion Losses at Electric-Vehicle Charging Stations," *IEEE Access*, vol. 6, pp. 26404–26415, 2018, doi: 10.1109/ACCESS.2018.2830187.

[14] M. Premkumar, C. Ramakrishnan, C. Kumar, R. Sowmya, T. R. Sumithira, and P. Jangir, "An Improved Quasi-Z-Source Boost DC-DC Converter Using Single-Stage Switched-Inductor Boosting Technique," *Machines*, vol. 10, no. 8, p. 669, Aug. 2022, doi: 10.3390/machines10080669.

[15] M. Dhananjaya, D. Potnuru, M. Premkumar, and H. H. Alhelou, "Design and Implementation of Single-Input-Multi-Output DC-DC Converter Topology for Auxiliary Power Modules of Electric Vehicle," *IEEE Access*, vol. 10, pp. 76975–76989, 2022, doi: 10.1109/ACCESS.2022.3192738.

[16] M. Premkumar, C. Kumar, A. Anbarasan, and R. Sowmya, "A novel non-isolated high step-up DC–DC boost converter using single switch for renewable energy systems," *Electrical Engineering*, vol. 102, no. 2, pp. 811–829, Jun. 2020, doi: 10.1007/s00202-019-00904-8.

[17] K. Mahmud, M. J. Hossain, and G. E. Town, "Peak-Load Reduction by Coordinated Response of Photovoltaics, Battery Storage, and Electric Vehicles," *IEEE Access*, vol. 6, pp. 29353–29365, 2018, doi: 10.1109/ACCESS.2018.2837144.

[18] V. Monteiro, J. G. Pinto, and J. L. Afonso, "Experimental Validation of a Three-Port Integrated Topology to Interface Electric Vehicles and Renewables with the Electrical Grid," *IEEE Transactions on Industrial Informatics*, vol. 14, no. 6, pp. 2364–2374, Jun. 2018, doi: 10.1109/TII.2018.2818174.

[19] A. K. Singh, A. K. Mishra, K. K. Gupta, P. Bhatnagar, and T. Kim, "An Integrated Converter with Reduced Components for Electric Vehicles Utilizing Solar and Grid Power Sources," *IEEE Transactions on Transportation Electrification*, vol. 6, no. 2, pp. 439–452, Jun. 2020, doi: 10.1109/TTE.2020.2998799.

[20] J. S. P. A. Venkata and S. S. Williamson, "Analysis and design of single-stage, two-mode AC/DC converters for on-board battery charging applications," *IET Power Electronics*, vol. 13, no. 4, pp. 830–843, Mar. 2020, doi: 10.1049/iet-pel.2019.0777.

[21] K. Jain, M. Gupta, and A. K. Bohre, "Implementation and Comparative Analysis of PO and INC MPPT Method for PV System," in *India International Conference on Power Electronics, IICPE*, Dec. 2018, pp. 1–6, doi: 10.1109/IICPE.2018.8709519.

[22] S. Mohanty, B. Subudhi, and P. K. Ray, "A new MPPT design using grey Wolf optimization technique for photovoltaic system under partial shading conditions," *IEEE Transactions on Sustainable Energy*, vol. 7, no. 1, pp. 181–188, Jan. 2016, doi: 10.1109/TSTE.2015.2482120.

[23] D. F. Teshome, C. H. Lee, Y. W. Lin, and K. L. Lian, "A modified firefly algorithm for photovoltaic maximum power point tracking control under partial shading," *IEEE Journal of Emerging and Selected Topics in Power Electronics*, vol. 5, no. 2, pp. 661–671, 2017, doi: 10.1109/JESTPE.2016.2581858.

[24] D. Yousri, S. B. Thanikanti, D. Allam, V. K. Ramachandaramurthy, and M. B. Eteiba, "Fractional chaotic ensemble particle swarm optimizer for identifying the single, double, and three diode photovoltaic models' parameters," *Energy*, vol. 195, p. 116979, Mar. 2020, doi: 10.1016/j.energy.2020.116979.

[25] O. Abdalla, H. Rezk, and E. M. Ahmed, "Wind driven optimization algorithm based global MPPT for PV system under non-uniform solar irradiance," *Solar Energy*, vol. 180, pp. 429–444, Mar. 2019, doi: 10.1016/j.solener.2019.01.056.

[26] S. Hadji, J.-P. Gaubert, and F. Krim, "Theoretical and experimental analysis of genetic algorithms based MPPT for PV systems," *Energy Procedia*, vol. 74, pp. 772–787, Aug. 2015, doi: 10.1016/j.egypro.2015.07.813.

[27] L. Guo, Z. Meng, Y. Sun, and L. Wang, "A modified cat swarm optimization based maximum power point tracking method for photovoltaic system under partially shaded condition," *Energy*, vol. 144, pp. 501–514, Feb. 2018, doi: 10.1016/j.energy.2017.12.059.

[28] M. Kermadi, V. J. Chin, S. Mekhilef, and Z. Salam, "A fast and accurate generalized analytical approach for PV arrays modeling under partial shading conditions," *Solar Energy*, vol. 208, pp. 753–765, Sep. 2020, doi: 10.1016/j.solener.2020.07.077.

[29] M. Joisher, D. Singh, S. Taheri, D. R. Espinoza-Trejo, E. Pouresmaeil, and H. Taheri, "A Hybrid Evolutionary-Based MPPT for Photovoltaic Systems under Partial Shading Conditions," *IEEE Access*, vol. 8, pp. 38481–38492, 2020, doi: 10.1109/ACCESS.2020.2975742.

[30] C. H. Basha and C. Rani, "Different Conventional and Soft Computing MPPT Techniques for Solar PV Systems with High Step-Up Boost Converters: A Comprehensive Analysis," *Energies*, vol. 13, no. 2, p. 371, Jan. 2020, doi: 10.3390/en13020371.

[31] J. P. Ram, D. S. Pillai, A. M. Y. M. Ghias, and N. Rajasekar, "Performance enhancement of solar PV systems applying P&O assisted Flower Pollination Algorithm (FPA)," *Solar Energy*, vol. 199, pp. 214–229, Mar. 2020, doi: 10.1016/j.solener.2020.02.019.

[32] L. Avila, M. De Paula, M. Trimboli, and I. Carlucho, "Deep reinforcement learning approach for MPPT control of partially shaded PV systems in Smart Grids," *Applied Soft Computing*, vol. 97, p. 106711, Dec. 2020, doi: 10.1016/j.asoc.2020.106711.

[33] N. Priyadarshi, S. Padmanaban, J. B. Holm-Nielsen, F. Blaabjerg, and M. S. Bhaskar, "An Experimental Estimation of Hybrid ANFIS-PSO-Based MPPT for PV Grid Integration under Fluctuating Sun Irradiance," *IEEE Systems Journal*, vol. 14, no. 1, pp. 1218–1229, Mar. 2020, doi: 10.1109/JSYST.2019.2949083.

[34] J. Sahoo, S. Samanta, and S. Bhattacharyya, "Adaptive PID Controller with P&O MPPT Algorithm for Photovoltaic System," *IETE Journal of Research*, vol. 66, no. 4, pp. 442–453, Jul. 2020, doi: 10.1080/03772063.2018.1497552.

[35] N. Priyadarshi, M. S. Bhaskar, P. Sanjeevikumar, F. Azam, and B. Khan, "High-power DC-DC converter with proposed HSFNA MPPT for photovoltaic based ultra-fast charging system of electric vehicles," *IET Renewable Power Generation*, pp. 1–13, Jun. 2022, doi: 10.1049/rpg2.12513.

[36] M. Premkumar *et al.*, "An enhanced Gradient-based Optimizer for parameter estimation of various solar photovoltaic models," *Energy Reports*, vol. 8, pp. 15249–15285, Nov. 2022, doi: 10.1016/j.egyr.2022.11.092.

[37] M. Premkumar *et al.*, "Improved Perturb and Observation Maximum Power Point Tracking Technique for Solar Photovoltaic Power Generation Systems," *IEEE Systems Journal*, vol. 15, no. 2, pp. 3024–3035, Jun. 2021, doi: 10.1109/JSYST.2020.3003255.

BIOGRAPHIES OF AUTHORS

G. Saikiran Reddy (iD) 🇬 SC ◐ was born in Raichur, India. He received a B.E. degree in electrical and electronics from Reva University, affiliated with Reva University Bengaluru, India, during 2015-2019, and an M.Tech. degree in Power Electronics from the Dayananda Sagar College of Engineering, Bengaluru, Karnataka, India. His field of interest is MPPT controllers and DC-DC power converters. He can be contacted at email: gsaikiranreddy485@gmail.com.

Prof. Dr. M. Premkumar (iD) 🇬 SC ◐ was born in Coimbatore, India. He received a B.E. degree in electrical and electronics engineering from the Sri Ramakrishna Institute of Technology, Coimbatore, in 2004, an M.E. degree in applied electronics from the Anna University of Technology, Coimbatore, in 2010, and the Ph.D. degree from Anna University, Chennai, India, in 2019. He is currently working as an Associate Professor with the Dayananda Sagar College of Engineering, Bengaluru, India. Also, he is a research fellow at the Institute of Power Engineering, Universiti Tenaga Nasional (UNITEN), Kajang, Malaysia. He has over 14 years of teaching experience. He has published over 110 technical articles in various national/international peer-reviewed journals, such as IEEE, Elsevier, and Springer, with over 2000 citations and an H-index of 24. He has published/granted seven patents by IPR, India, and IPR, Australia. His current research interests include optimization algorithms, including single-, multi-, and many-objectives for different real-world engineering design problems, power converters/inverters, PV parameter extraction, PV MPPT, PV array faults, smart grid and microgrids, BMS for electric vehicles, and non-isolated/isolated DC-DC converters for renewable energy systems and EVs. According to the report published by Stanford University in 2021, he is one of the 2% influential scholars, which depicts the 100000 top scientists in the world. He is a member of various professional bodies, such as IEEE, ISTE, and IAENG. He is also an editor/reviewer for leading journals of different publishers, such as IEEE, IET, Wiley, Taylor & Francis, Springer, and MDPI. He can be contacted at email: mprem.me@gmail.com.

Suraj Ravi (iD) 🇬 SC ◐ was born in Shimogs, India. He received a B.E. degree in electrical and electronics from SDM Institute of Technology, Ujire, affiliated with VTU University Belgaum, India, during 2015-2019, and is currently pursuing M.Tech. degree in Power Electronics from the Dayananda Sagar College of Engineering, Bengaluru, Karnataka, India. His field of interest is MPPT techniques, optimization algorithms, and DC-DC power converters. He can be contacted at email: surajravi771997@gmail.com.

Dr. Laith Abualigah (iD) 🇬 SC ◐ received a degree in computer information systems and a master's degree in computer science from Al al-Bayt University, Jordan, in 2011 and 2014, respectively, and the Ph.D. degree from the School of Computer Science, Universiti Sains Malaysia (USM), Malaysia, in 2018. He is currently an Associate Professor with the Computer Science Department, Prince Hussein Bin Abdullah Faculty for Information Technology, Al al-Bayt University, Mafraq 25113, Jordan. He is also affiliated with Department of Electrical and Computer Engineering, Lebanese American University, Byblos 13-5053, Lebanon, Hourani Center for Applied Scientific Research, Al-Ahliyya Amman University, Amman 19328, Jordan, MEU Research Unit, Middle East University, Amman 11831, Jordan, Applied Science Research Center, Applied Science Private University, Amman 11931, Jordan, School of Computer Sciences, Universiti Sains Malaysia, Pulau Pinang 11800, Malaysia, and School of Engineering and Technology, Sunway University Malaysia, Petaling Jaya 27500, Malaysia. According to the report published by Stanford University in 2020, he is one of the 2% influential scholars, which depicts the 100000 top scientists in the world. He has published more than 200 journal articles and books, which collectively have been cited more than 14238 times (H-index=56). His main research interests include arithmetic optimization algorithm (AOA), bio-inspired computing, nature-inspired computing, swarm intelligence, artificial intelligence, meta-heuristic modelling and optimization algorithms, evolutionary computations, information retrieval, text clustering, feature selection, combinatorial problems, optimization, advanced machine learning, big data, and natural language processing. He also serves as an Associate Editor for the Cluster Computing journal (Springer) and the Soft Computing journal (Springer). He can be contacted at email: aligah.2020@gmail.com.